———————————————————

This is the **accepted version** of the article:

———————————————————

This version is avaible at https://ddd.uab.cat/record/213088

One-pot Electrosynthesis of Multi-layered Magnetic Metallopolymer Nanocomposites[†]

B. Özkale,[a] E. Pellicer,[b] M. A. Zeeshan,[a] J. F. López-Barberá,[c] J. Nogués,[c] J. Sort,[d]* B. J. Nelson[a] and S. Pané[a]*

Researchers have been investigating various methodologies for fabricating well-defined, homogenous composites consisting of nanoparticles (NPs) dispersed in a matrix. The main challenges are to prevent particle agglomerations during fabrication and to obtain nanoparticles whose size distribution could be tuned on demand. One of the methods that can provide these features is electrodeposition. We report for the first time the fabrication of a thin magnetic multilayer nanocomposite film by electrodeposition from one bath containing both a monomer and metal salts. Cobalt and cobalt-nickel NPs were deposited on conductive polymer polypyrrole thin films using different electrodeposition potentials and times. Multilayer nanocomposite films were fabricated by subsequent electrodeposition of polymer and nanoparticle layers. Scanning electron microscopy analysis showed that a wide range of NPs (80 – 280 nm) could be synthesized by manipulating growth potentials and times. The NPs for both cobalt and cobalt-nickel were found to contain hexagonal close-packed (hcp) and face centered cubic (fcc) phases based on X-ray diffraction and selected area diffraction. Magnetic measurements proved that both the single and the multi-layered nanocomposites were magnetic at room temperature.

1 Introduction

Polymers have become essential materials in the fields of micro- and nanoelectromechanical systems (MEMS and NEMS, respectively). Due to their low density and flexibility, polymeric materials are not only employed as small components, but they can also serve as stamps for building blocks in MEMS and NEMS devices[1-6]. Functional parts such as micro pumps, valves or microfluidic channels are often made of polymers due to their mechanical properties, ease of fabrication, and low manufacturing costs[2]. Some of the most common MEMS and NEMS polymers are polydimethylsiloxane (PDMS), SU-8, polymethylmethacrylate (PMMA), parylene, and polyimide[2]. To extend their performance and functionality, many nanostructures such as nanotubes, nanosheets, and nanoparticles (NPs) have been incorporated in polymeric matrices to enhance their flexibility, mechanical, electrochemical or catalytic properties[7-11]. Polymer-matrix nanocomposite materials have been employed for a variety of applications such as energy harvesting, sensing and actuation, catalysis, and biocidal food packaging[8-12]. There is also interest in the fabrication of magnetic-field responsive polymer nanocomposites. Small components and parts made of magnetic materials are extensively used in transducers, microfluidic control systems, and drug delivery platforms. The interesting magnetic behaviour of nanostructures combined with the wide functionality of polymers has recently resulted in devices built of magnetic polymer nanocomposites (MPN). For example, Suter et al. demonstrated the fabrication of microcantilevers made of photocurable epoxy SU-8 containing superparamagnetic magnetite nanoparticles (SMNP)[13]. Kwon and co-workers have shown that it is possible to build microactuators with programmed anisotropy consisting of a poly(ethyleneglycol)diacrylate (PEGDA) matrix with dispersed

SMNP[14]. Sotiriou et al. have fabricated multi-layered plasmonic and phosphorescent superparamagnetic actuators made of PMMA matrices[15]. Some investigations are also being conducted on hydrogel-based magnetic nanocomposites. For example, Olsson et al. manufactured aerogel magnets and magnetic nanopapers using bacterial cellulose matrices filled with ferrimagnetic cobalt ferrite NPs[16].

Several approaches have been established to engineer MPN. The most commonly used method is *in-situ* polymerization in the presence of magnetic NPs[13, 14, 16]. However, these methods have several disadvantages. One of the most fundamental issues is the agglomeration of particles due to strong magnetic and physical interactions. In this case, complex chemical formulations containing dispersing agents are employed to avoid the formation of agglomerates. Other problems arise from the uneven distribution of filler NPs within the polymer matrix. To overcome these drawbacks, some nanocomposites are fabricated by alternating several times the deposition of the polymer followed by the deposition of the nanoparticles. Layer-by-layer deposition or spin coating combined with flame-synthesis deposition are among these methods[9, 15]. However such techniques require combination of sequential fabrication steps that increases the complexity of fabrication and costs[15,17]. Another technique for fabricating MPN is electrodeposition. By combining suitable anodic and cathodic deposition phases, MPN can be fabricated in a layer-by-layer manner from one bath containing both the monomer and metal salts. For this purpose, conductive polymers can be electrodeposited using positive potentials (anodic phase) with metallic NPs deposited at negative potentials (cathodic phase). This method offers several advantages like ease of operation, reduced costs, and precise control of dimensions and composition by manipulation of deposition potentials and time[18].

Among the conducting polymers, polypyrrole (Ppy) has been widely studied based on its high stability and good conductivity. Various metal (Cu, Ni, Au, Ag) NPs have been grown electrochemically on thin polypyrrole films[17-21]. In most of these cases, deposition of polymer and metal nanoparticles are performed using separate electrolytes. It has also been shown that nanocomposite fabrication can be conducted from a single electrolyte containing both the monomer and the metal salts[18, 19]. In addition, Ppy is an excellent substrate to control the size of the electrodeposited nanoparticles; varying sizes can be obtained by simply changing the thickness of the Ppy[17, 20]. However in all cases, only single layer nanocomposites were fabricated, and there have not been any reports on the fabrication of multi-layered composites by electrodeposition.

Here, we report one-pot electrochemical synthesis of multi-layered thin film magnetic nanocomposites. Cobalt and cobalt-nickel nanoparticles were electrodeposited on an electrochemically grown polypyrrole film by reverse pulse plating from an electrolyte containing both the metal salt and the pyrrole (Py) monomer. Multi-layered nanocomposites were fabricated by electrodeposition of alternating subsequent polymer and nanoparticle layers.

2 Results and Discussion

The nanocomposites were obtained by anodically electrodepositing an initial Ppy film on a gold substrate, followed by the cathodic electrodeposition of the metallic NPs. A pulse plating approach was employed and the pulses for all layers were fixed to 1 ms with a duty cycle of 50 %. The growth times given represent total deposition time (t_T) including the *on* (t_{ON}) and *off* (t_{OF}) times. The multi-layered samples were obtained by subsequently repeating the process several times. The fabrication steps are given in Fig. 1. Using the designed electroplating technique, it was possible to tune the number of layers in the nanocomposites.

2.1 Cyclic Voltammetry

In order to assess the growth conditions, cyclic voltammetry scans for the Co and Co-Ni baths were performed (Fig. 2). The oxidation peak for cobalt can be clearly seen in the Py-Co bath. However, for Py-CoNi, this peak is significantly smaller, suggesting that the dissolution of Co is much higher than that of CoNi. In addition, reduction for both metals starts at − 1 V, which was taken as the upper limit for electrodeposition. Ppy deposition potential was chosen to be +1 V.

2.2 Nanoparticle growth on polypyrrole thin films

The scanning electron microscopy (SEM) images showed that NPs were successfully grown on polypyrrole thin films for both baths. Fig. 3 shows selected SEM images for cobalt and cobalt-nickel NPs-polypyrrole bilayer nanocomposites.

Different electrodeposition conditions were investigated for the nanoparticle growth on Ppy, within the range of -2 V to -5 V. In order to keep the charge density similar in all cases, the deposition time was reduced for higher electrodeposition
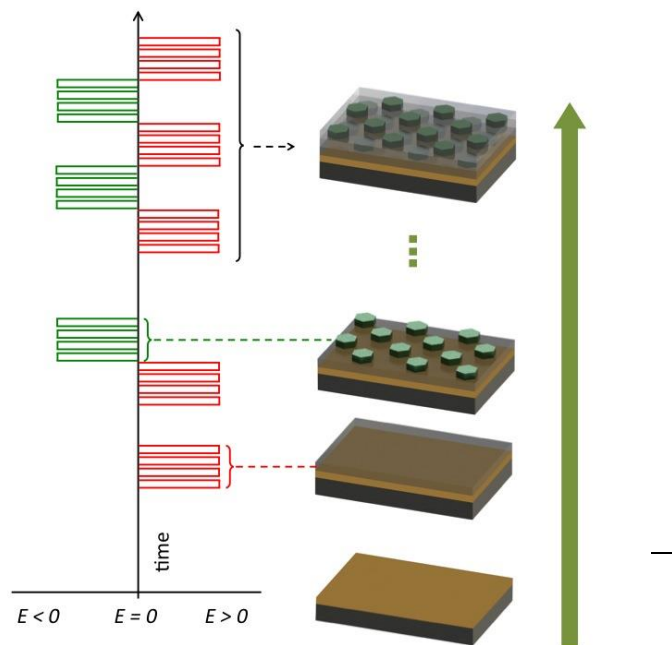

Fig. 1 Fabrication steps are shown for the multilayer nanocomposite. An initial layer of Ppy is achieved by pulse plating on gold coated silicon substrates. This is followed by the electrodeposition of metallic NPs. This procedure is performed multiple times to produce the multilayer nanocomposite. The pulses are not to scale and the rest phase introduced between Ppy and metallic NPs is not shown for simplicity.

potentials. By controlling the electrodeposition conditions it was possible to successfully tune the cobalt (Co) and cobalt-nickel (CoNi) average nanoparticle size from 60 to 250 nm (Table 1). As expected, for a given potential particle size typically decreases with decreasing deposition time (Fig. 3 (a) and (b)). However, such differences in size are not so evident when comparing very similar deposition times (c.f. average NP size for Co and CoNi at -3V for 1.1 s and 0.88 s) due to the inherent variability of the deposition process and fluctuations of current efficiency with time growth. At -2 V a combination of rounded and hexagonal star-like structures was found for both Co and CoNi NPs (Fig. 3 (c)). The occurrence of hexagonal star-like NPs was more pronounced for CoNi. Current efficiency also affected the particle size as noted in Fig. 3 (a) and (d), where deposition charge was kept almost constant but the deposition potential was more negative for Co (-5 V) than CoNi (-3 V). This is probably due to favoured H_2 evolution at higher potentials. Also, potentials higher than -3 V were not suitable for CoNi particle production due to increased hydrogen
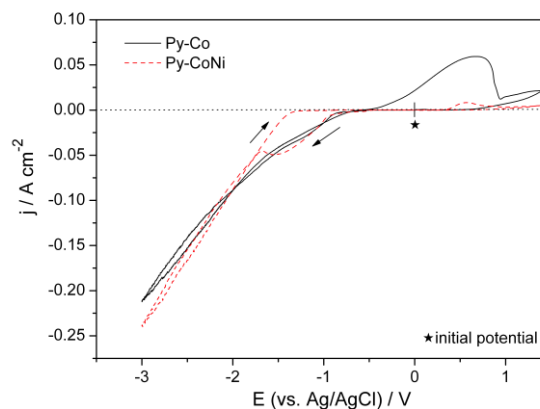

Fig. 2 Cyclic voltammetry (CV) scans for Py-Co (solid line) and Py-CoNi (dashed line) baths are shown. The scan limits were -3 V and 1.4 V, with a scan rate of 50 mV/s.

evolution. At -5 V H₂ evolution was greatly enhanced, and almost no deposition took place for CoNi particles since the current efficiency was very low. The particle size distributions for the conditions of Figure 3 are shown in Fig. S1.
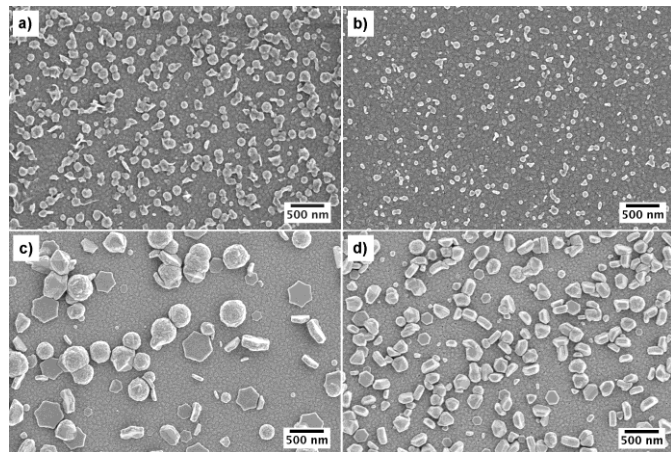

Fig. 3 SEM images taken with Inlens detector are shown for a) Co particles at -5V with 1 s total deposition time (0.52 C/cm²) b) Co particles at -5V with 0.4 s total deposition time (0.21 C/cm²) c) CoNi particles at -2V with 5.8 s total deposition time (0.93 C/cm²) and d) CoNi particles at -3V with 2.2 s total deposition time (0.46 C/cm²). In all cases, nanocomposites were grown by pulse plating using 1 ms pulse time and a duty cycle of 50 %.

EDX studies showed that the electrodeposition conditions can also be used to tailor the composition of CoNi NPs. For example, CoNi composition was found to be 46% cobalt and 54% nickel for particles produced at -2 V, whereas cobalt composition was decreased to 23% (77% nickel) at -3 V. A representative EDX spectrum is given in Fig. 4.

Table 1 Deposition conditions (applied potential and total deposition time) with the resulting approximate nanoparticle size are given. For all cases, pulse time was fixed to be 1 ms with a duty cycle of 50%. CoNi NPs could not be observed for all conditions and are not applicable (n.a.)

2.3 Fabrication of multilayer nanocomposite

The first attempts to grow multilayer nanocomposites were carried out using the Py – Co bath, from which successive layers of Ppy (deposition at 1V, t_T of 15 seconds) and Co NPs (deposition at -5 V, t_T of 1 second) were electrodeposited on gold – coated silicon substrates. Although bilayer Ppy – Co nanocomposites were fabricated successfully (Fig. 3 (a) and (b)) it was observed that the multilayer nanocomposite did not contain any NPs when analysed by FIB-SEM suggesting that Co NPs are mainly re-dissolved into the solution during growth. This is consistent with results obtained from the cyclic voltammetry scans (Fig. 2) in which during the anodic phase

Deposition potential (V)	Total deposition time (s)	Average Co NP size (nm)	Average CoNi NP size (nm)
-5	1	150	n.a.
-5	0.5	95	n.a.
-5	0.4	65	n.a.
-3	2.2	120	180
-3	1.1	65	130
-3	0.88	75	140
-2	5.8	140	240
-2	2.9	100	190
-2	1.45	70	n.a.

Co oxidation is very high leading to the re-dissolution of the Co NPs back into the bath during the anodic Ppy growth phase.

In order to avoid substantial re-dissolution of the metal counterpart during multilayer nanocomposite growth, fabrication was performed using the Py – CoNi bath, which shows a considerably smaller oxidation peak for CoNi than pure Co (Fig. 2). Fabrication using the Py – CoNi bath resulted in the successful growth of Ppy – CoNi NPs multi-layered nanocomposites from a single bath by electrodeposition (Fig. 5). In the nanocomposite cross-section shown in Fig. 5, subsequent CoNi NP layers separated by thin Ppy films can be clearly observed, and the presence of CoNi was confirmed by EDX (the particle was composed of 46% Co and 54% Ni). The multilayer thin films were approximately 700 nm thick on average. In all cases, it was observed that the average thickness of the different CoNi layers was similar, implying that CoNi NPs did not re-dissolve even for high Ppy deposition potentials.

Fig. 4 EDX spectrum for CoNi NPs fabricated -2 V for 5.8 seconds total deposition time. Silicon, gold, and titanium signals are received from the substrate whereas the cobalt and nickel signals are from the nanoparticles.
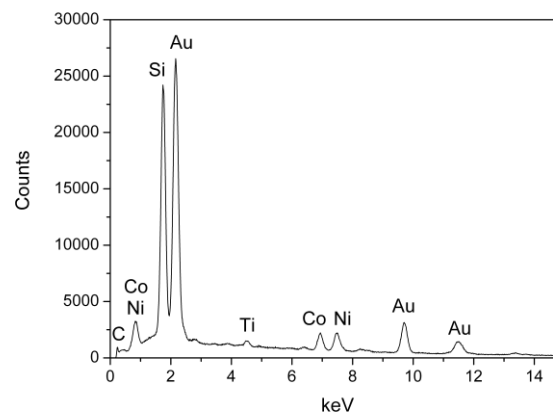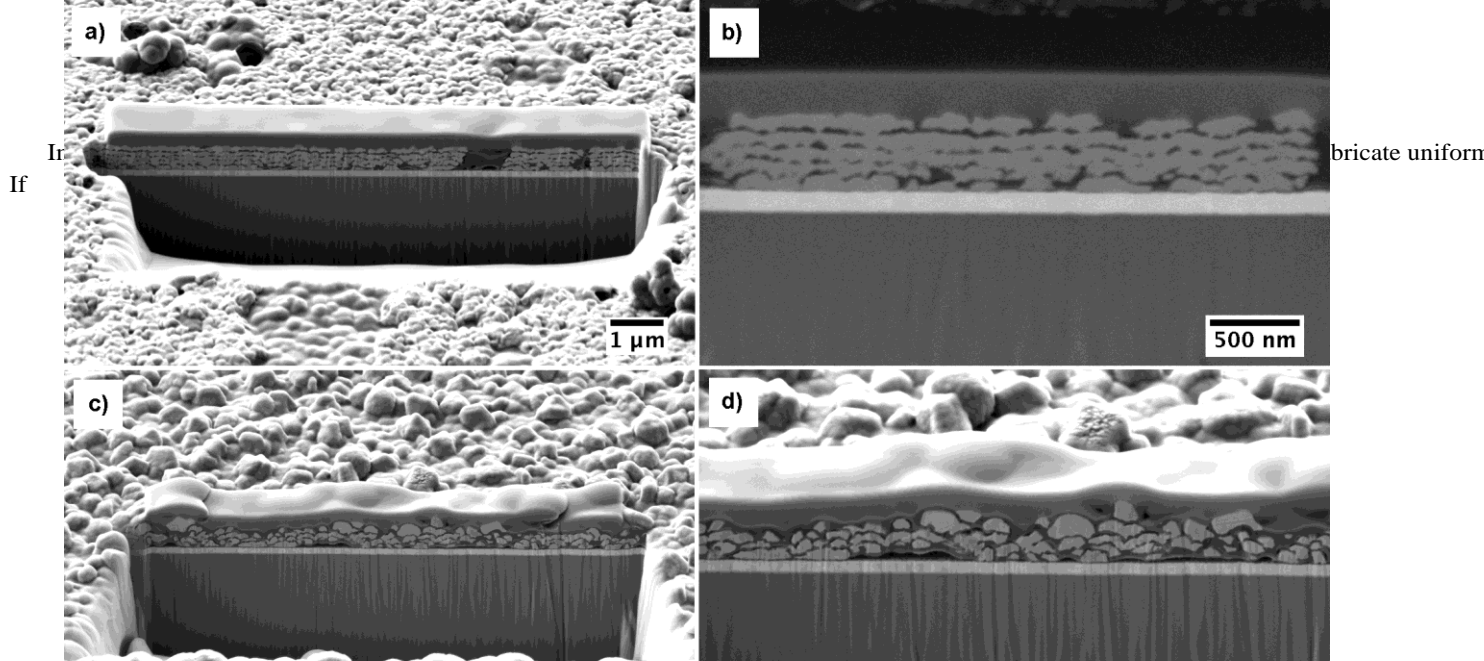
Fig. 3 Cross-section SEM imaging of multilayer CoNi – Ppy nanocomposites with five layers. Both samples (a-b, c-d) were fabricated at the same conditions with initial Ppy layer at 1V for 15 seconds, CoNi NPs at -2 V for 5.8 seconds and intermediate Ppy layers at 2 V for 0.75 seconds.

the rest phase was potentiostatically controlled, film detachment was observed probably due to slight bubble formation between the substrate and the growing thin film (Fig. S3). To avoid this, the electrochemical cell was programmed to automatically switch off during each rest phase.

In order to check the degree of coverage of CoNi NPs by the Ppy layer, Ppy deposition was carried out at two different potentials, 1 V and 2 V, with similar charge densities. It was seen that while the Ppy deposition at 1 V with relatively long deposition times was not sufficient to completely cover the NPs (Fig. S4), deposition at 2V resulted in a homogenous coverage. In order to assure the homogeneity of the Ppy layer, different total deposition times (0.75 – 24 seconds) at 2 V were studied. It was observed that the particles are completely covered with Ppy for all deposition times and did not get damaged during the deposition of Ppy due to re-dissolution issues. An example of such a sandwich type Ppy – CoNi nanocomposite with a thick secondary Ppy layer is shown in Fig. 6. It was also seen that thick layers of the secondary Ppy inhibited NP growth. Therefore, the secondary Ppy deposition potential was chosen to be 2 V with total deposition time as 0.75 s. The CoNi NPs were grown at -2 V for 5.8 seconds, which was chosen due to the reduced H_2 evolution during NP growth. This was found to be an important point for fabricating homogeneous and smooth nanocomposite films without defects. Additionally, as can be seen in Fig. 5, it was observed that the intermediate Ppy layers showed slight differences in thickness from sample to sample

prepared in the same conditions. The Ppy layer separating the particles is seen more clearly in c, d as opposed to a, b and
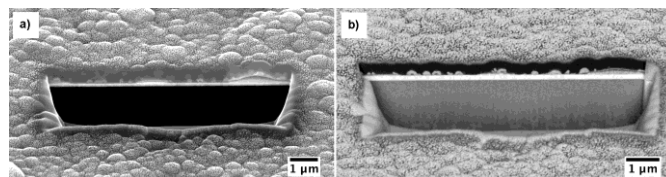

Fig. 6 Cross-section SEM images of a sandwich type CoNi – Ppy nanocomposite is shown for a) In-lens detector, b) ESB detector. The initial Ppy layer was deposited at 1 V, 15 seconds; followed by CoNi NPs deposition at -2 V, 5.8 seconds and a secondary layer of Ppy at 2 V, 7.5 seconds. Cross-sections were acquired and imaged with FIB-SEM where a carbon deposition was done at the site of the cut in order to provide a uniform cross-section. NPs which are consistent in size can be seen in the images which are covered with a thick Ppy layer of approximately 200 nm.

interconnections between particle layers are more frequent in the latter case. This is probably due to reduced efficiency of the Ppy electrodeposition which can be attributed to the slow decomposition of pyrrole in the bath due to air (which is commonly observed in pyrrole)[23]. The reduction in Ppy growth efficiency may cause thinner intermediate Ppy layers. The resulting thinner Ppy layer most probably creates "hot spots" of conductivity where CoNi electrodeposition efficiency is slightly higher, resulting in the observed interconnections. However, in both cases the Ppy and CoNi NPs layers can clearly be identified.
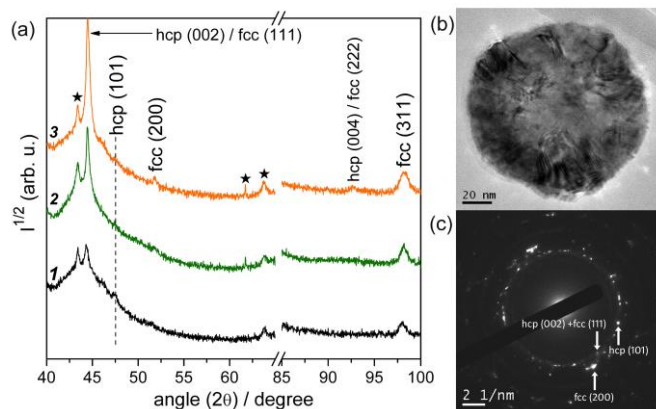
Fig. 7 (a) XRD patterns for (1) Co – Ppy bilayer nanocomposite electrodeposited at -2 V for 5.8 seconds (2) CoNi – Ppy bilayer nanocomposite electrodeposited at -2 V for 5.8 seconds (3) CoNi – Ppy multilayer (5 layers) nanocomposite electrodeposited at -2 V for 5.8 seconds for CoNi NPs and at -2V for 0.75s for secondary Ppy layers. The peaks indicated by an asterisk are for cobalt oxides; (b) TEM image showing a single particle in a CoNi – Ppy bilayer fabricated at -2 V for 2.9 seconds; (c) SAED pattern of the selected particle in (b).

XRD patterns showed a combination of an amorphous background arising from the Ppy layer and some reflections attributed to the metallic particles (Fig. 7). For the Co – Ppy bilayer nanocomposite the reflections belong to the hexagonal close-packed (hcp) phase, whereas for the bi- and multilayer CoNi – Ppy nanocomposites a mixture of face-centered cubic (fcc) and hcp phases is observed. The presence of both hcp and fcc phases is expected taking into account the chemical composition of the CoNi NPs which was determined by EDX to be 46 wt % Co and 54 wt % Ni [22]. The ratio between the intensities of the different hexagonal peaks implies that the particles exhibit some degree of texture. A slight shift in fcc peaks towards higher angles was observed for CoNi compared to the position of tabulated fcc Co, which proves that a solid solution was actually formed. The fcc (200) peak (which is not overlapped with any hcp peak) has been considered to calculate the cell parameter, a, of CoNi NPs. A value of a = 3.527 Å is obtained for both the bilayer and the multilayer. According to the Vegard's law [*Journal of The Electrochemical Society*, **157, 2010,** E92-E97], this value corresponds to a Ni percentage of around 50 at%, which matches the EDX data. The TEM image shown in Fig. 7 (b) presents a single CoNi NP featuring a rounded morphology for which crystallographic defects such as staking faults are visible. The nanoparticle is made up of hcp and fcc domains as can be seen in the corresponding SAED pattern (Fig. 7 (c)). Other particles showed the hexagonal star-like morphology as mentioned before (Fig. 3 (c)).

The literature suggests that the particle shape depends on the bath composition, deposition potential, and crystalline structure of resulting particles [24]. At low deposition potentials (e.g. -1.4 V) cobalt particles can grow in a hexagonal shape due to the preferential growth of hcp phases along the edges of the particles after nucleation [24]. The fact that the hexagonal particles are most clearly observed at -2 V for CoNi (Fig. 3 (c)), is probably due to the low deposition potential and their large size. In addition, the growth of perfectly spherical particles is most likely related to the presence of acetate in the bath which is reported to cause such particle geometry [24].

2.4. Magnetic properties

Measurements performed with vibrating sample magnetometer and (VSM) and magneto-optic Kerr effect (MOKE) prove that both bi- and multi-layered nanocomposites are ferromagnetic at room temperature. The hysteresis loops for the Co – Ppy and CoNi – Ppy bilayers are given in Fig. 8. In plane measurements for bilayer nanocomposites show that for Co (Fig. 8 (a)) coercivity (H_C) and saturation magnetization (M_S) are higher than for CoNi (Fig. 8 (b)). The decrease in saturation magnetization is expected since Ni (489.5 emu/cm^3) has a much lower M_s than Co (1426.8 emu/cm^3). Nevertheless, the existence of cobalt and/or nickel oxides cannot be ruled out. Notably, the measured values of M_S for Co (850 emu/cm^3) and CoNi (380 emu/cm^3), are approximately 40% of the tabulated values for hcp-Co and CoNi (taking into account the alloy composition $Co_{0.46}Ni_{0.54}$), which is in good agreement with the particle coverage observed by SEM (Fig. 3).

The difference in coercivity might be due to the presence of fcc phase in CoNi which has smaller magnetocrystalline anisotropy than the hcp phase [25]. However, other effects such as the presence of stacking faults may also play a role [26]. Additionally the coercivity values measured by VSM are lower than those measured by MOKE (Fig. 8 (a) and (b), inset). This could be due to dynamic effects since H_C may depend on the sweep rate of the magnetic field [27]. However, since MOKE is a local measurement (i.e., a few tens of microns laser spot), there could also be some local inhomogeneities between different particles (e.g., size, shape, orientation or phase) which could also explain the slight differences in H_c between VSM and MOKE. Nevertheless, in both techniques H_c is observed to be larger for Co than for CoNi. Out-of-plane (i.e., polar) hysteresis loops could not be recorded for Co or CoNi – Ppy bilayer layer nanocomposites. This is thought to be related to shape anisotropy (i.e., platelet- like shapes for some particles) which would favor in-plane easy axis for the magnetization.

For the CoNi – Ppy multilayer nanocomposite, both in-plane and out-of-plane hysteresis loops could be measured (Fig. 8 (c)). The shapes of the loops reveal that the multilayer nanocomposite does not have a clear easy axis (in-plane or out-of-plane preferred orientation for the magnetization). The coercivity in the loop measured perpendicular to plane (H_c = 200 Oe) is slightly higher than in the one in-plane (H_c = 110 Oe). In turn, the squareness ratio is M_R/M_S = 0.15 for out-of-plane orientation and M_R/M_S = 0.25 for in-plane orientation. This lack of a clear easy axis is the consequence of the competition between the shape anisotropy arising from the flat (i.e., star shaped hexagonal NPs) geometry of the particles (which would tend to orient the magnetization in the film plane) and the magnetocrystalline anisotropy. XRD results reveal crystallographic texture along the (001) direction (c-axis) of the hcp phase and the (111) direction of the fcc phase (Fig. 7). In fact, these are the magnetic easy axis directions for hcp-Co and

fcc-Ni. Hence, shape anisotropy likely favors in-plane orientation of the magnetization while magnetocrystalline anisotropy probably favors an out-of-plane easy axis. As a result, none of the two loops is particularly square.
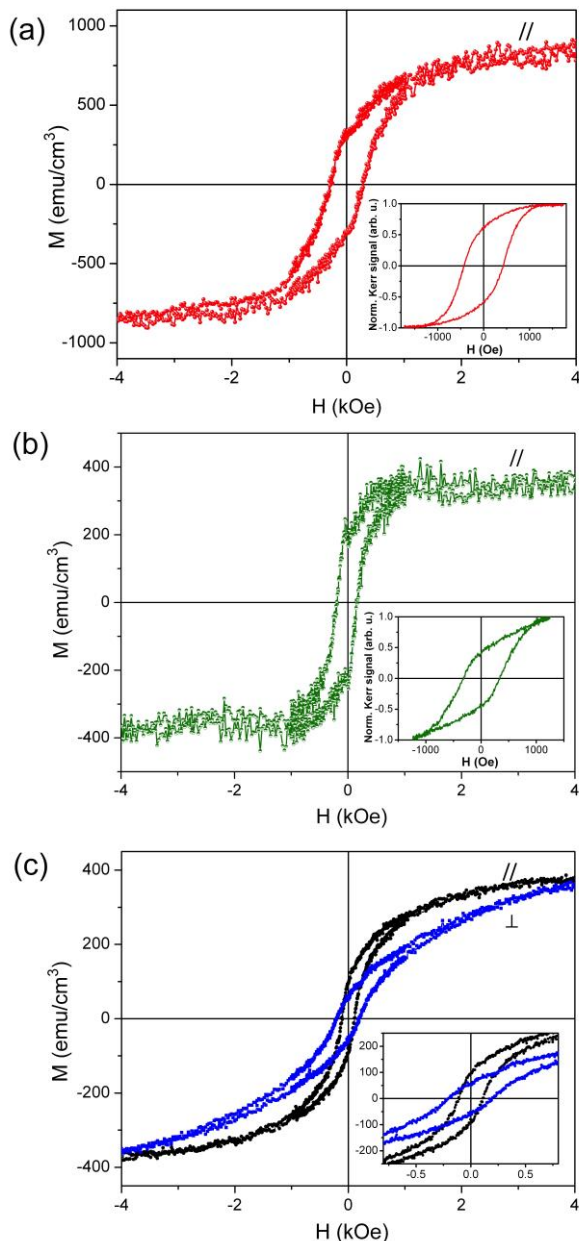

Fig. 8 In-plane hysteresis loops for (a) Co – Ppy bilayer, (b) CoNi – Ppy bilayer, and (c) in-plane and out-of-plane hysteresis loops CoNi – Ppy multilayer (5 layers) nanocomposites. The insets in (a) and (b) show the hysteresis loops measured with MOKE and in (c) an enlarged view at low fields. Note that the nanoparticles for the three systems were grown at -2 V for 5.8 s.

It is also likely that magnetic dipolar (or exchange) inter-particle interactions can affect the coercivity and squareness ratio of the measured samples, particularly in regions where the particles are very close to each other (dipolar) or in direct contact (exchange) [DIP]. In this sense, the reduction of coercivity and squareness ratio in the CoNi-Ppy multilayer (Fig. 8c) measured along the film plane, as compared to the CoNi-Ppy bilyaer (Fig. 8b), could also be ascribed to the stronger dipolar interactions between the particles in the former.

3 Experimental Details

3.1 Electrochemical Synthesis of Nanocomposites

The nanocomposites were grown on gold substrates by using a standard three-electrode set up. A gold coated silicon substrate with an area of 0.25 cm^2 was selected as the working electrode. Silicon wafers (4-inch) were e-beam evaporated with 25 nm of titanium and 125 nm of gold, which were later diced into 1x0.5 cm chips. The counter electrode was a pure platinum wire, and the reference electrode was Ag.AgCl (3M KCl). All electrochemical experiments were done using an Autolab PGSTAT302N potentiostat. A nitrogen blanket covered the solution during electrodeposition to minimize oxidation of pyrrole due to air.

Experiments were conducted with two different electrolytes; compositions are given in Table 2. Chemicals were received from Sigma Aldrich with analytical grade purity. Pyrrole was distilled prior to use as well as every 6 months and kept at 4°C, under N$_2$. Adjustment of pH was done using *para*-toluene sulfonic acid. Electrodeposition for both baths was performed under N$_2$ circulation and with constant stirring.

Initial polypyrrole layer was grown at 1 V using a total deposition time of 15 seconds. For the multi-layer nanocomposites, intermediate polypyrrole layers were electrodeposited at 2 V with the total deposition time as 0.75 seconds. Cobalt (Co) and cobalt-nickel (CoNi) NPs were grown at various potentials (-2 V, -3 V, -5 V) and deposition times (0.5 to 5.8 seconds). For both anodic and cathodic cycles pulse times were fixed at 1 ms and the duty cycle was 50%.

Table 2 Components and composition for the two electrolytes are given.

Component/Condition	Bath 1	Bath 2
Pyrrole	0.1 M	0.1 M
Cobalt acetate	0.15 M	0.03 M
Nickel sulfamate tetrahydrate	-	0.12 M
Sodium para-toluene sulfonate	0.49 M	0.49 M
Ethanol	25 vol. %	25 vol. %
pH	2.5	2.5
Temperature	33°C	33°C

3.2 Characterization of Nanocomposites

SEM imaging was done with Inlens and SE2 detectors at 2 kV. FIB-SEM imaging was also done at the same conditions.

Nanoparticle size was determined for each condition using the image analysis software ImageJ. Three images per condition was analysed on average and an average value for nanoparticle size was calculated.

For cutting the cross sections a gallium ion source was used with currents of 300 pA-1.5 nA. Samples were sputtered with a thin layer of gold prior to SEM and FIB-SEM. A thin carbon

coating was deposited during imaging prior to FIB cross-sectioning to provide smooth cuts. EDX analysis was done using 20 kV and was coupled to the FIB-SEM (Zeiss NVision 40).

X-ray diffraction patterns (XRD) were acquired on a Philips X'Pert Pro in the 40°-100° 2θ range using CuKα radiation with 0.025° of step size and 10 seconds of holding time.

Hysteresis loops were recorded at room temperature using a vibrating sample magnetometer (VSM), from Oxford Instruments, both along the in-plane and perpendicular-to-plane directions, applying a maximum field of 4 kOe. Local magnetic measurements were performed using a magneto-optic Kerr effect (MOKE) setup, from Durham Magneto-Optics, with a maximum in-plane applied field of 1500 Oe.

4 Conclusions

Multilayer metallopolymer magnetic nanocomposites were fabricated by electrodeposition from a single bath. A bath containing both pyrrole monomer and metal salts (Co and CoNi) was used. The results demonstrate the first successful growth of multilayer nanocomposites using Ppy and CoNi NPs. Magnetic measurements using VSM and MOKE show that both bilayer and multilayer nanocomposites are strongly magnetic at room temperature.

Acknowledgements

Notes and references

[a] Multi-Scale Robotics Lab, Institute of Robotics and Intelligent Systems, ETH Zurich, 8092 Zurich, Switzerland, E-mail: spane@ethz.ch
[b] Departament de Física, Facultat de Ciències, Universitat Autònoma de Barcelona, Campus UAB, 08193 Bellaterra, Spain.
[c] Institució Catalana de Recerca i Estudis Avançats (ICREA) and Departament de Física, Universitat Autònoma de Barcelona, Campus UAB 08193 Bellaterra, Spain. Jordi.Sort@uab.cat
[d] ICN2 Institut Catala de Nanociencia i Nanotecnologia, Campus UAB, Bellaterra, 08193, Barcelona, Spain and Institució Catalana de Recerca i Estudis Avançats (ICREA), Barcelona, Spain.

† Electronic Supplementary Information (ESI) available: [Details on fabrication of multilayer nanocomposites]. See DOI: 10.1039/b000000x/

1 C.-Y. Chen, C.-H. Chen, T.-Y. Tu, C.-M. Lin, A. M. Wo, *Lab on a Chip*, 2011, **11**, 733.

2 C. Liu, *Advanced Materials*, 2007, **19**, 3783.

3 S. Elhadj, R. M. Rioux, M. D. Dickey, J. J. DeYoreo, G. M. Whitesides, *Nanoletters*, 2010, **10**, 4140.

4 B. Xu, F. Arias, G. M. Whitesides, *Advanced Materials*, 1999, **6**, 492.

5 H. Schröder, L. Hoffmann, J. Müller, P. Alhorn, M. Fleger, A. Neyer, C. M. Niemeyer, *Small*, 2009, **5**, 1547.

6 J. K. Gansel, M. Thiel, M. S. Rill, M. Decker, K. Bade, V. Saile, G. Freymann, S. Linden, M. Wegener, *Science*, 2009, **325**, 1513.

7 C. Meng, C. Liu, L. Chen, C. Hu, S. Fan, *Nanoletters*, 2010, **10**, 4025.

8 Z. Song, T. Xu, M. L. Gordin, Y.-B. Jiang, I.-T. Bae, Q. Xiao, H. Zhan, J. Liu, D. Wang, *Nanoletters*, 2012, **12**, 2205.

9 F. Hua, T. Cui, Y. M. Lvov, *Nanoletters*, 2004, **4**, 823.

10 M. K. Shin, G. M. Spinks, S. R. Shin, S. I. Kim, S. J. Kim, *Advanced Materials*, 2009, **21**, 1712.

11 C.-H. Zhu, Z.-B. Hai, C.-H. Cui, H.-H. Li, J.-F. Chen, S.-H. Yu, *Small*, 2012, **6**, 930.

12 A. Kubacka, C. Serrano, M. Ferrer, H. Lunsdorf, P. Bielecki, M. L. Cerrada, M. F. Garcia, M. F. Garcia, *Nanoletters*, 2007, **7**, 2529.

13 M. Suter, O. Ergeneman, J. Zürcher, C. Moitzi, S. Pané, T. Rudin, S. E. Pratsinis, B. J. Nelson, C. Hierold, *Sensors and Actuators B*, 2011, Article in press.

14 J. Kim, S. E. Chung, S.-E. Choi, H. Lee, J. Kim, S. Kwon, *Nature Materials*, 2011, **10**, 747.

15 G. A. Sotiriou, C. O. Blattmann, S. E. Pratsinis, *Advanced Functional Materials*, 2012, **22**, 1.

16 R. T. Olsson, M. A. S. A. Samir, G. Salazar-Alvarez, L. Belova, V. Ström, L. A. Berglund, O. Ikkala, J. Nogués, U. W. Gedde, *Nature Nanotechnology*, 2010, **5**, 584.

17 S. Srivastava , N. A. Kotov, Acc. Chem. Res. 2008, **41**, 1831.

17 X. J. Zhou, A. J. Harmer, N. F. Heinig, K. T. Leung, *Langmuir*, 2004, **20**, 5109.

18 T. Rapecki, M. Donten, Z. Stojek, *Electrochemistry Communications*, 2010, **12**, 624.

19 Y. Haseko, N. K. Shrestha, S. Teruyama, T. Saji, *Electrochimica Acta*, 2006, **51**, 3652.

20 D. K. Sarkar, X.J. Zhou, A. Tannous, M. Louie, K.T. Leung, *Solid State Communications*, 2003, **125**, 365.

21 S. Jing, S. Xing, L. Yu, C. Zhao, *Materials Letters*, 2007, **61**, 4528.

22 O. Ergeneman, K. M. Sivaraman, S. Pané, E. Pellicer, A. Teleki, A. M. Hirt, M. D. Baró, B. J. Nelson, *Electrochimica Acta*, 2011, **56**, 1399.

23 L. R. Anderson, K. Liu, *Pyrrole and Pyrrole Derivatives* Kirk-Othmer Encyclopedia of Chemical Technology, John Wiley and Sons, Inc., 2000.

24 L. M. A. Monzon, K. Rode, M. Venkatesan, J. M. D. Coey, *Chemistry of Materials*, 2012, **24**, 3878.

25 Y. Sato, T. Nishiyama, M. Ohtake, F. Kirino, M. Futamoto, *IEEE Transactions on Magnetics*, 2010, **46**, 349.

[DIP] D. Kechrakos, K. N. Trohidou, *Phys. Rev. B*, 1998, **58**, 12169.

26 J. Sort, S. Suriñach, J. S. Muñoz, M. D. Baró, M. Wojcik, E. Jedryka, S. Nadolski, N. Sheludko, J. Nogués, *Physical Review B*, 2003, **68**, 014421.

27 Y. Pennec, J. Camarero, J. C. Toussaint, S. Pizzini, M. Bonfim, F. Petroff, W. Kuch, F. Offi, K. Fukumoto, F. Nguyen Van Dau, J. Vogel, *Physical Review B*, 2004, **69**, 180402(R).